

SRG/eROSITA-triggered *XMM-Newton* observations of three Be/X-ray binaries in the LMC: Discovery of X-ray pulsations

F. Haberl¹, C. Maitra¹, D. Kaltenbrunner¹, D.A.H. Buckley^{2,3}, I.M. Monageng^{2,3}, A. Udalski⁴, V. Doroshenko⁵, L. Ducci⁵, I. Kreykenbohm⁶, P. Maggi⁷, A. Rau¹, G. Vasilopoulos⁷, P. Weber⁶, and J. Wilms⁶

¹ Max-Planck-Institut für extraterrestrische Physik, Gießenbachstraße 1, 85748 Garching, Germany, e-mail: fwh@mpe.mpg.de

² South African Astronomical Observatory, PO Box 9, Observatory Rd, Observatory 7935, South Africa

³ Department of Astronomy, University of Cape Town, Private Bag X3, Rondebosch 7701, South Africa

⁴ Astronomical Observatory, University of Warsaw, Al. Ujazdowskie 4, 00-478, Warszawa, Poland

⁵ Institut für Astronomie und Astrophysik, Sand 1, 72076 Tübingen, Germany

⁶ Remeis Observatory and ECAP, Universität Erlangen-Nürnberg, Sternwartstraße 7, 96049 Bamberg, Germany

⁷ Université de Strasbourg, CNRS, Observatoire astronomique de Strasbourg, UMR 7550, 67000 Strasbourg, France

Received 28 December 2022 / Accepted 23 January 2023

ABSTRACT

Context. Using data from eROSITA, the soft X-ray instrument aboard *Spectrum-Roentgen-Gamma* (SRG), we report the discovery of two new hard transients, eRASSU J050810.4–660653 and eRASSSt J044811.1–691318, in the Large Magellanic Cloud. We also report the detection of the Be/X-ray binary RX J0501.6–7034 in a bright state.

Aims. We initiated follow-up observations to investigate the nature of the new transients and to search for X-ray pulsations coming from RX J0501.6–7034.

Methods. We analysed the X-ray spectra and light curves from our *XMM-Newton* observations, obtained optical spectra using the South African Large Telescope to look for Balmer emission lines and utilised the archival data from the Optical Gravitational Lensing Experiment (OGLE) for the long-term monitoring of the optical counterparts.

Results. We find X-ray pulsations for eRASSU J050810.4–660653, RX J0501.6–7034, and eRASSSt J044811.1–691318 of 40.6 s, 17.3 s, and 784 s, respectively. The H α emission lines with equivalent widths of -10.4 \AA (eRASSU J050810.4–660653) and -43.9 \AA (eRASSSt J044811.1–691318) were measured, characteristic for a circumstellar disc around Be stars. The OGLE I- and V-band light curves of all three systems exhibit strong variability. A regular pattern of deep dips in the light curves of RX J0501.6–7034 suggests an orbital period of ~ 451 days.

Conclusions. We identify the two new hard eROSITA transients eRASSU J050810.4–660653 and eRASSSt J044811.1–691318 and the known Be/X-ray binary RX J0501.6–7034 as Be/X-ray binary pulsars.

Key words. galaxies: individual: LMC – X-rays: binaries – stars: emission-line, Be – stars: neutron pulsars: individual: eRASSU J050810.4–660653, eRASSSt J044811.1–691318, RX J0501.6–7034

1. Introduction

The soft X-ray instrument eROSITA on board the *Spektrum-Roentgen-Gamma* (SRG) mission (Predehl et al. 2021) began scanning the sky in great circles in December 2019. Until December 2021, one full eROSITA sky survey was completed every half-year (eRASS1 to eRASS4), whereas eRASS5 was stopped in February 2022. The survey strategy with scans along great circles (six per day), which intersect at the ecliptic north and south poles leads to a higher number of scans across sources near the poles. The Large Magellanic Cloud (LMC) is located sufficiently close to the south-ecliptic pole to have the north-eastern side scanned for up to three weeks.

The first scans from eRASS1 imaged the northern part of the LMC, leading to the discovery of eRASSU J050810.4–660653 (Haberl et al. 2020) and eRASSU J052914.9–662446 (Maitra et al. 2020a). Following its discovery, eRASSU J052914.9–662446 was observed with *NuSTAR* and pulsations in the X-ray flux were discovered (Maitra et al. 2020b). The results of a detailed analysis are presented in Maitra et al. (2023). One year later, eRASSU J050810.4–660653 was seen to have brightened

and we executed an anticipated target of opportunity (ToO) observation with *XMM-Newton*, which allowed us to discover X-ray pulsations (Haberl et al. 2021). The source became brightest at the end of eRASS4/beginning of eRASS5 when it was detected by Mikhail Pavlinsky ART-XC (Pavlinsky et al. 2021), the hard X-ray instrument on board SRG. A *NuSTAR* observation independently revealed the pulsations of eRASSU J050810.4–660653 (Salganik et al. 2022).

Over the course of eRASS3, when eROSITA was scanning over RX J0501.6–7034, the source was found in a bright state, whereas it was not detected during eRASS1 and eRASS2. In particular, RX J0501.6–7034 is known since it was discovered with the *Einstein* observatory (CAL 9; Long et al. 1981) and identified as a Be/X-ray binary (Crampton et al. 1985; Cowley et al. 1984). The cited authors suggested the variable star SV* HV 2289 as optical counterpart and found H β in emission in their blue spectrum which indicates a B0e spectral type. We again triggered an *XMM-Newton* ToO observation with the aim to confirm the identification and detect pulsations.

Another new transient X-ray source with a hard spectrum (eRASSSt J044811.1–691318) was found during eRASS4 on the

western side of the LMC towards the Magellanic Bridge. As a possible optical counterpart, we identified a star with colour and brightness consistent with a B star, suggesting a Be/X-ray binary suitable for an *XMM-Newton* follow-up observation.

In this paper, we describe the results from our X-ray observations of eRASSU J050810.4–660653, RX J0501.6–7034, and eRASSt J044811.1–691318, using eROSITA, *XMM-Newton*, and Swift. These results are detailed in Sect. 2. In Sect. 3, we present the identification of the optical counterparts, their long-term monitoring recorded by the Optical Gravitational Lensing Experiment (OGLE; Udalski et al. 2008, 2015) and optical spectra (Sect. 3.1) obtained with the South African Large Telescope (SALT; Buckley et al. 2006). We discuss our final results in Sect. 4 and conclusions in Sect. 5.

2. X-ray observations and data analysis

2.1. eROSITA

To analyse the data, we used the eROSITA Standard Analysis Software System (eSASS Brunner et al. 2022) version eSASSusers_211214. To produce eROSITA source products like light curves and spectra, we used the eSASS task `srctool` (see e.g. Maitra et al. 2021; Haberl et al. 2022a). We defined circular regions to extract source (radius 50'', 60'', and 40'') and background events (from a nearby source-free region; radius 50'', 90'', and 65'') for eRASSU J050810.4–660653, RX J0501.6–7034, and eRASSt J044811.1–691318, respectively. For the spectra and light curves, we selected all valid pixel patterns (PATTERN = 15). For the light curves, we combined the data from all cameras (telescope modules TM 1–7) and applied a cut in the fractional exposure of 0.15 (FRACEXP > 0.15) to exclude data from the edge of the detectors. We created combined spectra using only data from TM 1–4 and 6, the five cameras with an on-chip filter. We note that TM5 and TM7 suffer from a light leak (Predehl et al. 2021) and no reliable energy calibration is available yet. The eROSITA source spectra were binned to a minimum of one count per bin to use Cash statistics (Cash 1979).

The eROSITA light curves of eRASSU J050810.4–660653, RX J0501.6–7034, and eRASSt J044811.1–691318 are shown in Figs. A.1, A.2, and A.3. eRASSU J050810.4–660653 is located closest to the south-ecliptic pole and was scanned most often, including the first part of eRASS5 in total 272 times, while eRASSt J044811.1–691318 in the west of the LMC was scanned 134 times. The light curves of eRASSU J050810.4–660653 and RX J0501.6–7034 show variability by a factor of a few on timescales of weeks and between surveys. eRASSt J044811.1–691318 was detected only during eRASS4 and too faint to draw conclusions about variability over days.

The analysis of the eROSITA spectra (and also *XMM-Newton* EPIC spectra, see below) was performed using XSPEC v12.10.1f (Arnaud 1996). We fitted the eROSITA spectra using a simple absorbed power-law model with two absorption components, one accounting for the foreground absorption in the Galaxy with ISM abundances following Wilms et al. (2000) and atomic cross-sections from Verner et al. (1996). The Galactic column density, $N_{\text{H}}^{\text{Gal}}$, was taken from Dickey & Lockman (1990) and fixed in the fits (4.4 , 8.6 and $7.2 \times 10^{20} \text{ cm}^{-2}$ for eRASSU J050810.4–660653, RX J0501.6–7034, and eRASSt J044811.1–691318, respectively). For the absorption along the line of sight through the LMC and local to the source, we fixed the elemental abundances at 0.49 solar (Rolleston et al.

2002; Luck et al. 1998) and left the column density free in the fit. Errors on spectral fit parameters indicate 90% confidence intervals throughout the paper.

We started to fit the eROSITA spectra of eRASSU J050810.4–660653 from the five epochs individually. The best-fit parameters are assembled in Table 1 (upper part) and indicate no significant changes in spectral shape (column density or power-law index) with time. The overall flux varies by a factor of 6.3 (4.0–13.4). Given the constant spectral shape, we next fitted the spectra simultaneously using a common absorption and power-law index (Table 1, second part). In this case the flux varies by a factor of 7.4 (5.9–9.5). The power-law index is typical for HMXBs observed in the 0.2–10 keV band (Haberl et al. 2008) and the X-ray luminosity varied between 0.5 and $3.6 \times 10^{36} \text{ erg s}^{-1}$ on the half-year timescale defined by the eROSITA surveys.

RX J0501.6–7034 was also detected in each of the first four eRASS surveys, but at a fainter flux level. Therefore, we fitted the four eROSITA spectra simultaneously with common power-law index and absorption. No significant LMC absorption was required in the fit. The best-fit parameters are listed in Table 1.

eRASSt J044811.1–691318 was only detected during eRASS4 and we used the corresponding spectrum for our spectral analysis (Table 1). Although it is not very well constrained, the derived power-law index indicates a harder X-ray spectrum compared to the other two sources. Again, no significant LMC absorption was required, but column densities up to 10^{22} cm^{-2} cannot be ruled out. The luminosity was at a similar level as seen from RX J0501.6–7034 and at the lower luminosity range covered by eRASSU J050810.4–660653. The eROSITA spectra with their best-fit models are plotted in Fig. 1.

2.2. XMM-Newton

We triggered *XMM-Newton* follow-up observations from our anticipated ToO programs for the three targets (see Table 2). We used the *XMM-Newton* Science Analysis Software (SAS) 19.1.0¹ package to process the data from the European Photon Imaging Camera (EPIC), which is equipped with pn- (Strüder et al. 2001) and MOS-type (Turner et al. 2001) charge-coupled device (CCD) detectors. From the processed EPIC event files, we created such products as images, spectra, and light curves using the SAS task `evselect`.

We performed a maximum likelihood source detection simultaneously on the 15 images from the three EPIC instruments in five energy bands (0.2–0.5 keV, 0.5–1 keV, 1–2 keV, 2–4.5 keV, and 4.5–12 keV) as described in Sturm et al. (2013). The resulting X-ray positions are listed in Table 2.

We extracted energy spectra from circular regions around source (radius 40'', 45'', and 30'') and nearby background (radius 60'', 60'', and 50'') for eRASSU J050810.4–660653, RX J0501.6–7034, and eRASSt J044811.1–691318, respectively. Events with PATTERN 1–4 for EPIC-pn (Strüder et al. 2001) and PATTERN 1–12 for EPIC-MOS (Turner et al. 2001) were selected, applying the conservative event filtering with FLAG 0 for EPIC-pn and EPIC-MOS. The EPIC source spectra were binned to a minimum of 20 counts per bin to use Gaussian statistics and the response files were computed with the SAS tasks `arfgen` and `rmfgen`.

In modelling the EPIC spectra, we followed the same approach as for the eROSITA spectra with a power law with two absorption column densities as basic model. This model ade-

¹ <https://www.cosmos.esa.int/web/xmm-newton/sas>

Table 1. Analysis of eROSITA spectra.

eRASS ^(a)	Power-law index	$N_{\text{H}}^{\text{LMC}(b)}$ 10^{20} cm^{-2}	$F_{\text{x}}^{(c)}$ 10^{-12} $\text{erg cm}^{-2} \text{s}^{-1}$	$L_{\text{x}}^{(d)}$ 10^{36} erg s^{-1}
eRASSU J050810.4–660653				
0–1	1.2 ± 0.4	$30.0^{+23.5}_{-17.6}$	$3.0^{+1.1}_{-0.8}$	$1.03^{+0.28}_{-0.19}$
1–2	0.8 ± 0.4	$11.5^{+17.4}_{-11.5}$	$1.8^{+0.7}_{-0.6}$	$0.57^{+0.20}_{-0.15}$
2–3	$1.07^{+0.23}_{-0.20}$	$17.8^{+9.5}_{-7.5}$	$6.1^{+1.2}_{-1.0}$	$2.00^{+0.31}_{-0.26}$
3–4	$0.98^{+0.23}_{-0.20}$	$11.4^{+10.1}_{-7.6}$	$4.7^{+1.0}_{-0.8}$	$1.52^{+0.26}_{-0.21}$
4–5	0.97 ± 0.13	$12.9^{+5.1}_{-4.5}$	$11.4^{+1.3}_{-1.2}$	3.7 ± 0.3
eRASSU J050810.4–660653 simultaneous fit C-statistic = 1216; $\chi^2 = 1511$; d.o.f. = 1510 ^(e)				
0–1			$3.2^{+0.5}_{-0.4}$	$1.04^{+0.14}_{-0.13}$
1–2			$1.52^{+0.24}_{-0.22}$	0.49 ± 0.07
2–3	1.00 ± 0.10	$14.5^{+3.8}_{-3.5}$	6.4 ± 0.6	$2.07^{+0.18}_{-0.17}$
3–4			4.7 ± 0.5	$1.53^{+0.15}_{-0.14}$
4–5			$11.2^{+1.0}_{-0.9}$	$3.63^{+0.27}_{-0.25}$
RX J0501.6–7034 simultaneous fit C-statistic = 352.6; $\chi^2 = 363.3$; d.o.f. = 426 ^(e)				
1			$0.10^{+0.07}_{-0.06}$	$0.031^{+0.024}_{-0.019}$
2	$1.10^{+0.24}_{-0.14}$	<7	$0.22^{+0.11}_{-0.09}$	$0.070^{+0.035}_{-0.028}$
3			$2.05^{+0.37}_{-0.41}$	$0.66^{+0.13}_{-0.11}$
4			$2.60^{+0.48}_{-0.50}$	$0.83^{+0.07}_{-0.13}$
eRASSt J044811.1–691318 eRASS4 C-statistic = 76.2; $\chi^2 = 82.9$; d.o.f. = 89 ^(e)				
4	$0.7^{+1.0}_{-0.6}$	<102	$1.8^{+1.2}_{-0.9}$	$0.59^{+0.34}_{-0.20}$

Notes. ^(a) For the definition of the observing epochs see the Appendix. ^(b) The total absorption column consists of $N_{\text{H}}^{\text{Gal}}$, which is fixed to the Galactic foreground with solar abundances, and $N_{\text{H}}^{\text{LMC}}$, which accounts for the additional absorption component within the LMC. ^(c) Observed flux in the energy range of 0.2–8 keV. ^(d) Corresponding unabsorbed luminosity assuming a source distance of 50 kpc. ^(e) Best-fit Cash statistics with corresponding χ^2 value and degrees of freedom (d.o.f.).

quately fits the spectra from eRASSU J050810.4–660653. However, the residuals from the fit to the spectra of RX J0501.6–7034 reveal a systematic pattern that indicates a second emission component. We added a black-body component which was also used for other BeXRBs (e.g. Haberl et al. 2022b). Also, the fit to the spectra of eRASSt J044811.1–691318 suggests that the pure power-law model is too simple, but the low statistical quality of the spectrum prevents a more detailed spectral study. The derived best-fit parameters for the three sources are summarised in Table 3 and the spectra with best-fit model are shown in Fig. 2.

Correcting the event arrival times to the solar system barycentre and relaxing the selection to valid pixel patterns (PATTERN 1–12), we created EPIC-pn light curves in the 0.2–8.0 keV energy band from the same extraction regions as used for the spectra. For our search for X-ray pulsations in the light curves, we first created power spectra which revealed pulsations for all our three targets. The power spectra obtained

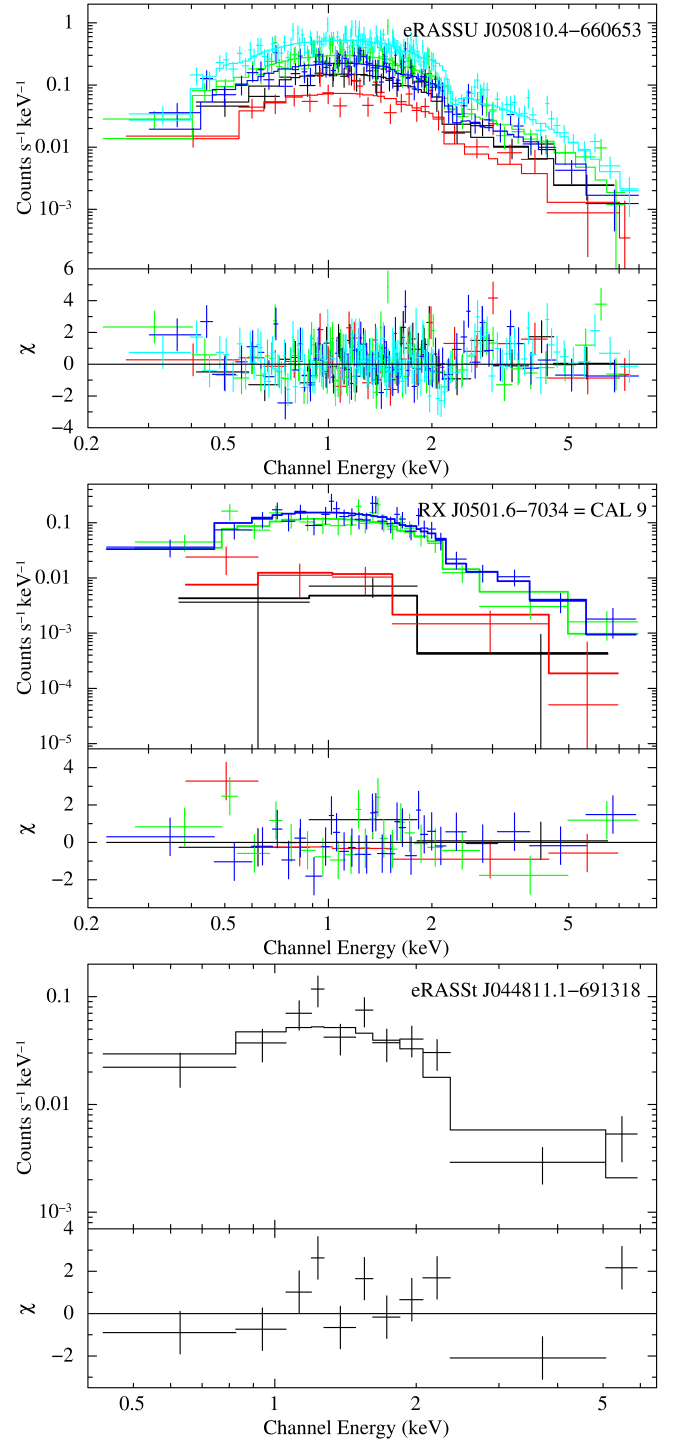


Fig. 1. eROSITA spectra of eRASSU J050810.4–660653 (top), RX J0501.6–7034 (middle), and eRASSt J044811.1–691318 (bottom) together with their best-fit models (as histograms). The respectively lower panels show the residuals from the best-fit model divided by the 1σ errors. For eRASSU J050810.4–660653, the simultaneous spectral fit to the spectra of the different epochs defined in Fig. A.1 is shown (epoch 1 marked in black, epoch 2 in red, epoch 3 in green, epoch 4 in blue, and epoch 5 in turquoise). For RX J0501.6–7034 the simultaneous fit to the spectra of eRASS1 (black), eRASS2 (red), eRASS3 (green), and eRASS4 (blue) is presented. Finally, the eRASS4 spectrum of eRASSt J044811.1–691318 is shown at the bottom.

from the 0.2–8.0 keV EPIC-pn light curves are presented in Fig. 3. The power spectrum of eRASSU J050810.4–660653 with

Table 2. *XMM-Newton* observations of eRASSU J050810.4–660653, RX J0501.6–7034, and eRASSSt J044811.1–691318.

Source name	Obs. ID	Observation time	Exposure time pn, MOS1, MOS2 (s)	R.A. (J2000) (h m s)	Dec. (° ' ")	Err 1 σ (")
eRASSU J050810.4–660653	0860800301	2020-12-17 09:54 – 19:24	19500, 31779, 32332	05 08 09.99	-66 06 51.6	0.51
RX J0501.6–7034 (CAL 9)	0883950101	2021-05-18 00:30 – 08:57	20300, 24743, 24617	05 01 23.66	-70 33 34.0	0.51
eRASSSt J044811.1–691318	0883950201	2021-11-29 01:59 – 08:22	16383, 21075, 21424	04 48 10.67	-69 13 18.0	0.52

Notes. The net exposure times after background-flare screening are listed for pn, MOS1 and MOS2, respectively. The positional errors include the statistical (1 σ) and a systematic error of 0.5" (see [Sturm et al. 2013](#)), added quadratically.

Table 3. EPIC X-ray timing and spectral analysis results.

Source (short)	Period ^a (s)	N _H ^{LMC} (10 ²⁰ cm ⁻²)	Photon index	kT (keV)	Flux ^b (erg cm ⁻² s ⁻¹)	L _x ^{b,c} (erg s ⁻¹)	χ^2_r /dof
J0508	40.602544 ± 7.2×10 ⁻⁵	8.0 ± 1.5	0.76 ± 0.02	–	5.62×10 ⁻¹²	1.74×10 ³⁶	0.96/1107
J0501 ^d	17.3321 ± 3.8×10 ⁻³	<2.5	1.20 ^{+0.12} _{-0.07}	1.61 ^{+0.17} _{-0.13}	2.88×10 ⁻¹²	9.01×10 ³⁵	1.00/729
J0448	783.75 ± 0.55	13.4 ± 6.2	0.80 ± 0.06	–	1.02×10 ⁻¹²	3.19×10 ³⁵	1.40/186

Notes. ^(a) Most probable period with 1 σ error. ^(b) X-ray flux and luminosity in the 0.2–10 keV band. ^(c) Absorption-corrected luminosity assuming a distance of 50 kpc. ^(d) To model the spectra of RX J0501.6–7034 an additional black-body component was included. It contributes 36.7% to the total flux and 35.3% to the luminosity. The χ^2_r for the fit without the black-body component was 1.10 for 731 degrees of freedom (dof). The F-test probability of 3.2×10⁻¹⁶ justifies the addition of this component.

Table 4. Optical counterparts of eRASSU J050810.4–660653, RX J0501.6–7034, and eRASSSt J044811.1–691318.

Source (short)	V ^a (mag)	Q ^{a,b} (mag)	2MASS	J (mag)	H (mag)	K _s (mag)	R.A. (J2000) ^c (h m s)	Dec. (° ' ")	D ^d (")
J0508	14.15	-0.89	05080993–6606523	13.98	13.93	13.70	05 08 09.94	-66 06 52.1	0.61
J0501	14.36	-0.84	05012419–7033346	13.98	13.17	13.06	05 01 23.84	-70 33 33.9	0.95
J0448	15.77	-0.76	–	–	–	–	04 48 10.65	-69 13 17.0	0.99

Notes. ^(a) Magnitudes and colours are taken from [Zaritsky et al. \(2004\)](#) or in the case of eRASSSt J044811.1–691318 from [Massey \(2002\)](#). ^(b) Reddening-free parameter, defined as Q = U-B - 0.72(B-V). For the distribution of the Q parameter of BeXRBs in the SMC; see [Haberl & Sturm \(2016\)](#). ^(c) Position of the optical counterpart from Gaia EDR3 (see [Gaia Collaboration et al. 2021, 2016](#)). ^(d) Angular distance between *XMM-Newton* and Gaia position.

five harmonics of the fundamental frequency indicates a complex pulse profile. The power spectra of the other two pulsars, RX J0501.6–7034 and eRASSSt J044811.1–691318, only reveal their fundamental frequencies.

To determine the precise period and its error we applied in a second step the Bayesian approach described by [Gregory & Loredo \(1996\)](#) in a restricted frequency range around the fundamental frequency, which was determined from the power spectrum. This method was used already for other HMXB pulsars in the Magellanic Clouds (e.g. [Haberl et al. 2022b](#); [Vasilopoulos et al. 2017, 2013](#); [Haberl et al. 2008](#)).

The derived periods of the three new pulsars with their 1 σ errors are listed in Table 3. We folded the light curves with the most probable period and show the pulse profiles in Fig. 4. The pulse profile of eRASSU J050810.4–660653 is highly structured with a deep minimum. This dip is barely resolved in time and lasts $\lesssim 0.15$ in phase. The statistical quality of the pulse profile from RX J0501.6–7034 is low. It is characterised by a main peak of triangular shape and an indication for a second smaller peak.

Similarly, eRASSSt J044811.1–691318 shows a main peak with fast rise preceded by a smaller one.

3. Optical counterparts

We identified stars with V-magnitudes between 14.1 and 15.8 as optical counterparts for the three HMXB candidates, based on the values given in the Magellanic Cloud Photometric Survey (MCPS) of [Zaritsky et al. \(2004\)](#). Two of them also have entries in the Two Micron All Sky Survey (2MASS; [Skrutskie et al. 2006](#)) catalogue. In all three cases, the counterpart is found within the 2- σ error circle of the X-ray position (Tables 2 and 4). Furthermore, no other star brighter than V=17 mag and colours compatible with an early-type star is found within 10". The brightness and colours (Table 4), together with the X-ray spectral and temporal properties strongly suggest a Be/X-ray binary nature for all three objects.

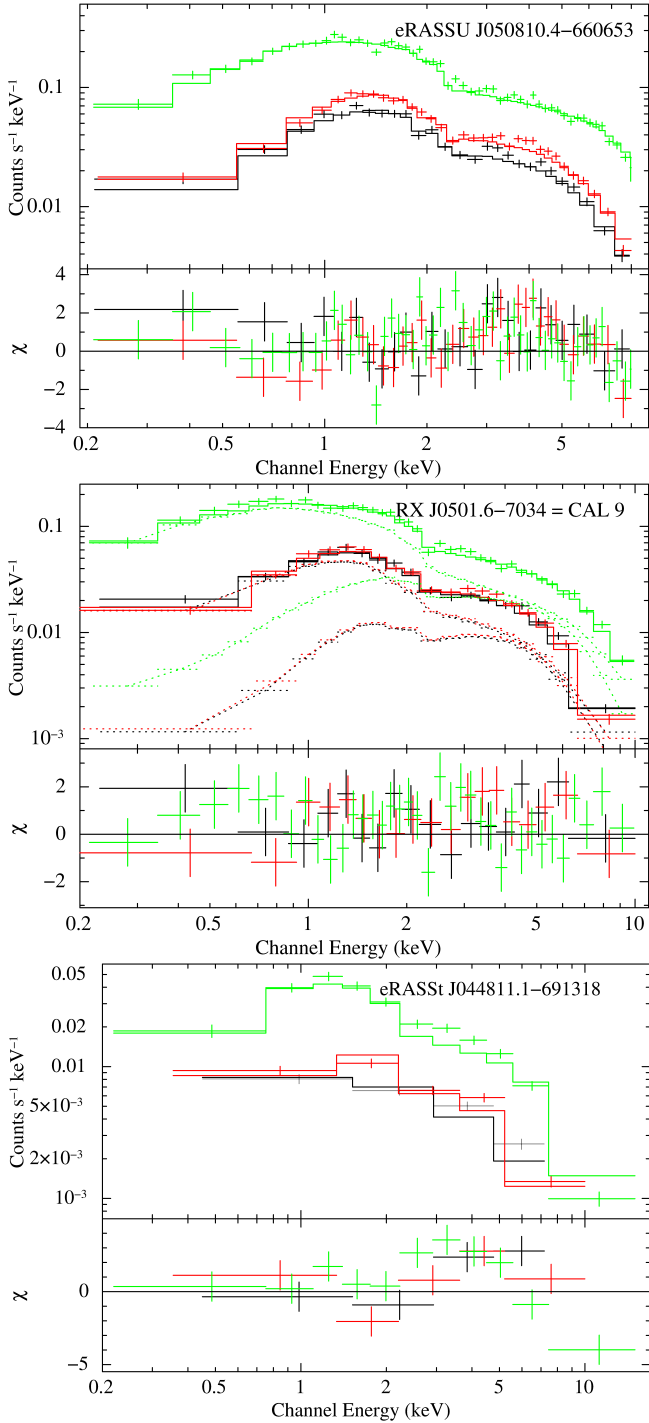


Fig. 2. EPIC spectra of the three new Be/X-ray binary pulsars (MOS1: black, MOS2: red, pn: green). The best-fit models are plotted as histogram and the bottom panels show the residuals. For eRASSU J050810.4–660653 and eRASSSt J044811.1–691318 an absorbed power law yielded an acceptable fit; however, for RX J0501.6–7034, an additional black-body component was included (individual components are indicated by dotted lines). See Table 3, for the model parameters.

3.1. SALT spectroscopy

We obtained optical spectra from eRASSU J050810.4–660653 and eRASSSt J044811.1–691318 using the Robert Stobie Spectrograph (RSS; Burgh et al. 2003) on SALT. To investigate the $H\alpha$ line, the PG0900 VPH grating was used, which covered the

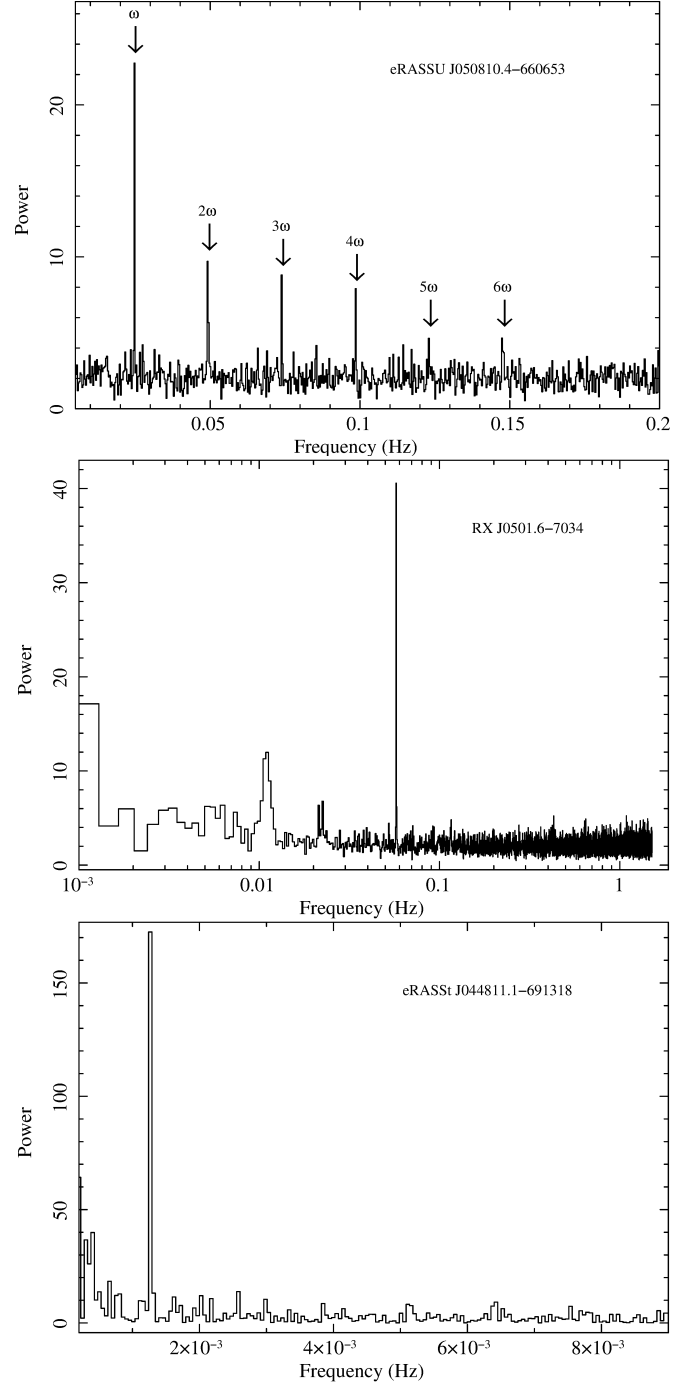


Fig. 3. Power spectra obtained from the EPIC-pn data (0.2–8.0 keV). *Top:* Pulsations from eRASSU J050810.4–660653 are clearly detected with a fundamental frequency of 0.0246 Hz corresponding to a period of 40.60 s together with signals at five harmonic frequencies. *Middle:* RX J0501.6–7034 shows pulsations with a frequency of about 57.7 mHz (17.3 s). *Bottom:* Longest period is detected from eRASSSt J044811.1–691318 at ~784 s (frequency of 1.28 mHz).

spectral region 3920–7000 Å at a resolution of 6.2 Å. The observations were conducted under the SALT transient follow-up program and are detailed in Table 5.

The RSS spectra are presented in Fig. 5. Both sources show a single-peaked $H\alpha$ emission line, which dominates the spectrum and is suggestive for a low to intermediate inclination angle of the Be disc. Also, $H\beta$ was seen in emission in both spectra. The measured equivalent width (EW) and full

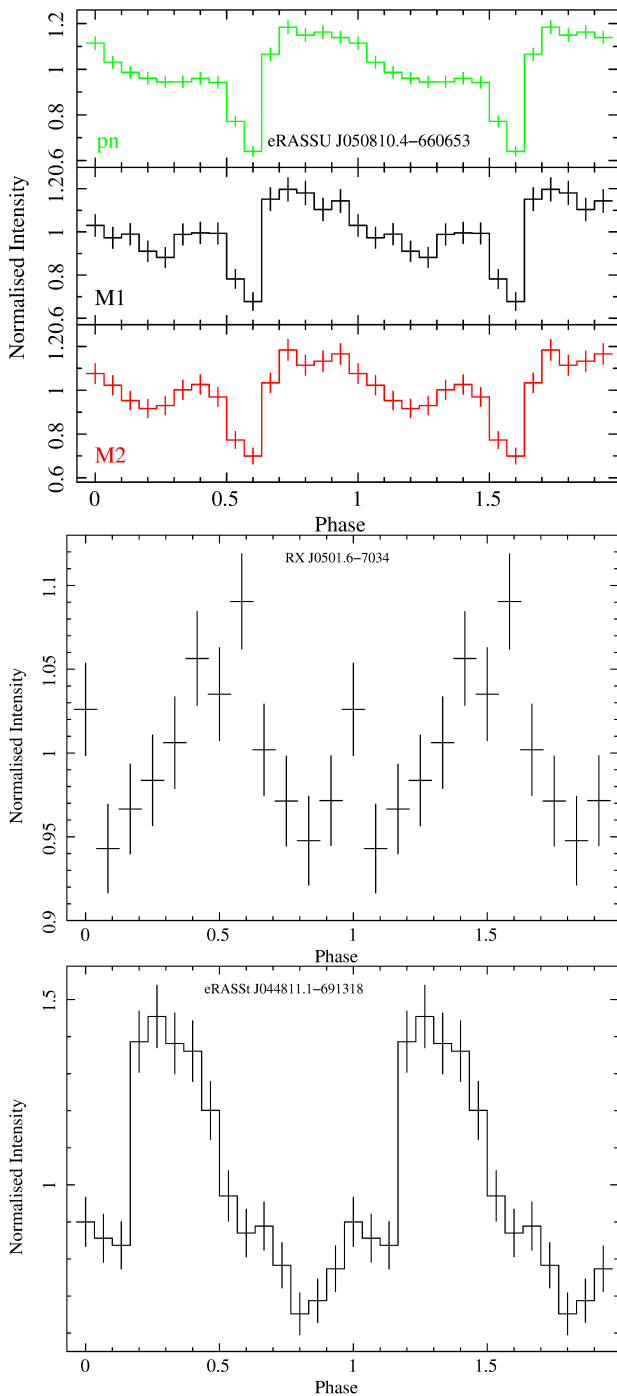


Fig. 4. Pulse profiles of our three targets obtained from the EPIC instruments in the 0.2–8.0 keV band. *Top:* For eRASSU J050810.4–660653, the profiles from all three EPIC instruments (MOS1: black, MOS2: red, pn: green) are compared. The pulse profiles from RX J0501.6–7034 (*middle*) and eRASSU J044811.1–691318 (*bottom*) were derived from EPIC-pn data.

width at half maximum (FWHM) of the $H\alpha$ lines seen from eRASSU J050810.4–660653 and eRASSU J044811.1–691318 are summarised in Table 5. In particular, the very strong $H\alpha$ line measured for eRASSU J044811.1–691318 indicates a large circum-stellar disc (Grundstrom & Gies 2006) and a long orbital period (Reig et al. 1997). Together with RX J0501.6–7034, which was identified as Be star previously (Negueruela & Coe 2002; Schmidtke et al. 1994), this also confirms

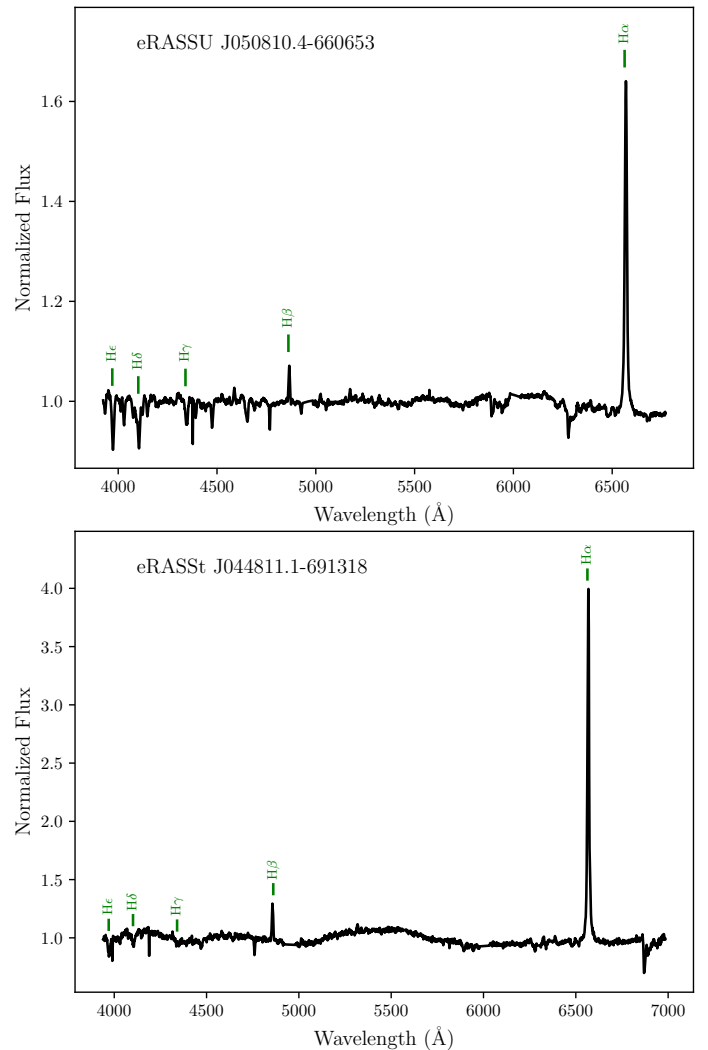


Fig. 5. Optical spectra of eRASSU J050810.4–660653 (top) and eRASSU J044811.1–691318 (bottom) taken with the RSS on SALT. The rest frame wavelengths of the Balmer lines are marked.

eRASSU J050810.4–660653 and eRASSU J044811.1–691318 as Be/X-ray binary pulsars.

3.2. OGLE monitoring

The optical counterparts of the three new Be/X-ray binary pulsars were monitored regularly as part of the OGLE project. Images were taken in the I- and V-band with the photometric magnitudes calibrated to the standard VI system. For all our three targets, their I- and V-band light curves are available, for eRASSU J050810.4–660653 during phase IV of the OGLE project (ten years of monitoring; see Fig. 6) and for RX J0501.6–7034 and eRASSU J044811.1–691318 during OGLE phases III and IV (in total 19.5 years, Fig. 7). Table 6 lists the OGLE IDs of the optical counterparts.

The OGLE light curves of eRASSU J050810.4–660653 show large oscillations, initially by nearly one magnitude in I. The time between the first two deepest minima is ~ 420 days. The decay in brightness after the second maximum seems to have stopped half way and the behaviour changed to much smaller brightness variations of ~ 0.1 mag in I. These two phases in the light curves can also be identified in the V-I colour index, which is plotted in the top panel of Fig. 8. During the initial phase the

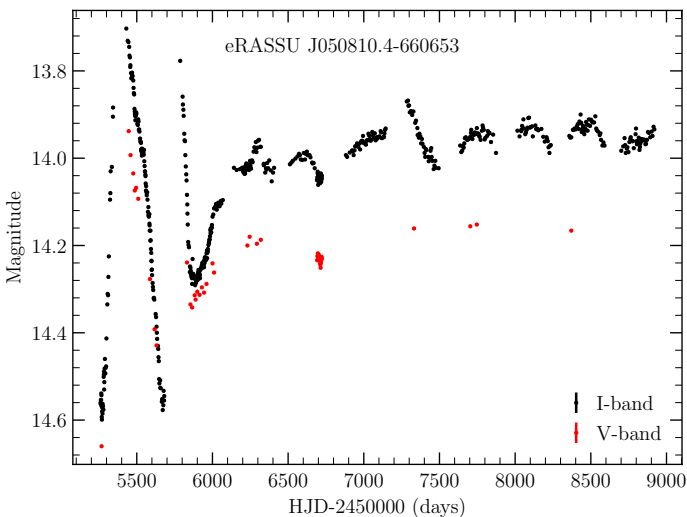
Table 5. SALT spectroscopy of eRASSU J050810.4–660653 and eRASSt J044811.1–691318.

Source name	Observation start (UTC)	Exposure (s)	EW (H α) (Å)	FWHM (H α) (Å)
eRASSU J050810.4–660653	2020-03-21 18:17:52	900	-10.42 ± 0.50	13.27 ± 0.10
eRASSt J044811.1–691318	2021-12-14 20:09:42	1600	-43.9 ± 1.4	9.70 ± 0.23

Table 6. OGLE monitoring of eRASSU J050810.4–660653, RX J0501.6–7034, and eRASSt J044811.1–691318.

Source name	OGLE III		OGLE IV	
	I-band	V-band	I-band	V-band
eRASSU J050810.4–660653	–	–	LMC512.20.12	LMC512.20.v.2
RX J0501.6–7034	LMC129.2.19005	LMC129.2.v.22055	LMC508.31.16128	LMC508.31.v.22929
eRASSt J044811.1–691318	LMC142.3.163	LMC142.3.v.52	LMC531.23.22017	LMC531.23.v.27359

colour index decreases, that is, the system gets bluer when fading in I. During the second phase, the system brightens again and returns to a redder colour. However, it did not reach the maximum brightness again and the colour ended up even redder than at the beginning of the light curve. In other words, the slopes of the paths in the V-I versus I plane were different during the two phases.

**Fig. 6.** OGLE-IV I- (black) and V-band (red) light curve of eRASSU J050810.4–660653 between 2010 March 5 and 2020 March 11.

A similar behaviour is seen in the OGLE light curves of RX J0501.6–7034. Large brightness variations by up to ~ 1 mag in the I band occurred several times with six deep minima during the OGLE monitoring period. The timescale between the deep minima is ~ 450 days, also very similar to eRASSU J050810.4–660653. The V-I colour index during the steep brightness declines became also bluer and returned to red during brightening in a closed loop as shown in Fig. 8 (middle panel).

The optical counterpart of eRASSt J044811.1–691318 is fainter and the largest variation was a 0.22 mag brightness decrease into a minimum with following recovery, which, unfortunately, was not fully covered by the OGLE observations. The V-I colour index does not follow such well-defined paths as in

the other two systems, but eRASSt J044811.1–691318 is also redder when brighter (Fig. 8, bottom panel).

The strong variations in the OGLE I-band light curve of RX J0501.6–7034 (Fig. 7, top) follow a regular pattern. We conducted a Lomb-Scargle (LS) periodogram analysis (Lomb 1976; Scargle 1982) in the range of 20–1000 days to check for a periodic behaviour. The strongest peak in the LS periodogram (Fig. 9) is indeed found at 450.7 days. However, the deep dips in the light curves do not occur strictly periodic: some are shifted to earlier phases and some to later ones.

4. Discussion

We analysed X-ray and optical data of three HMXB candidates in the LMC. Two of them, eRASSU J050810.4–660653 and eRASSt J044811.1–691318, were discovered as new hard X-ray transients in eROSITA data, while RX J0501.6–7034 was known from observations with the *Einstein* observatory and *ROSAT* as candidate for a Be/X-ray binary (Long et al. 1981; Schmidtke et al. 1994). The arc-second accuracy of the *XMM-Newton*/EPIC positions allowed us to uniquely identify the optical counterparts of the new transients and confirm the association of the suggested counterpart SV* HV 2289 with RX J0501.6–7034. Their X-ray spectral and temporal properties, together with the long-term behaviour of optical brightness and colours of the counterparts, and, lastly, the existence of H α emission, confirm all three objects as Be/X-ray binaries.

In addition, the analysis of the EPIC light curves revealed X-ray pulsations with periods of 40.6 s, 17.3 s, and 783.8 s, for eRASSU J050810.4–660653, RX J0501.6–7034, and eRASSt J044811.1–691318, respectively. The spin period distribution in the Small Magellanic Cloud (SMC) shows a remarkable bimodality with peaks at ~ 10 s and ~ 200 s and a minimum at ~ 25 –40 s (Haberl & Sturm 2016; Knigge et al. 2011). Although the number of known HMXB pulsars in the LMC (27 including the new discoveries from this work; Haberl et al. 2022b, who had already included eRASSU J050810.4–660653) is still significantly lower than in the SMC (68), such a minimum is not obvious for the LMC. Figure 10 compares the cumulative spin period distributions of the known HMXBs in the Magellanic Clouds. The relative abundance of pulsars with spin periods between ~ 10 s and ~ 100 s is higher in the LMC. However, a statistical two-sample Kolmogorov-Smirnov test reveals only a difference of the cumulative distributions at the $\sim 1 \sigma$ level and more LMC systems are required to confirm the difference.

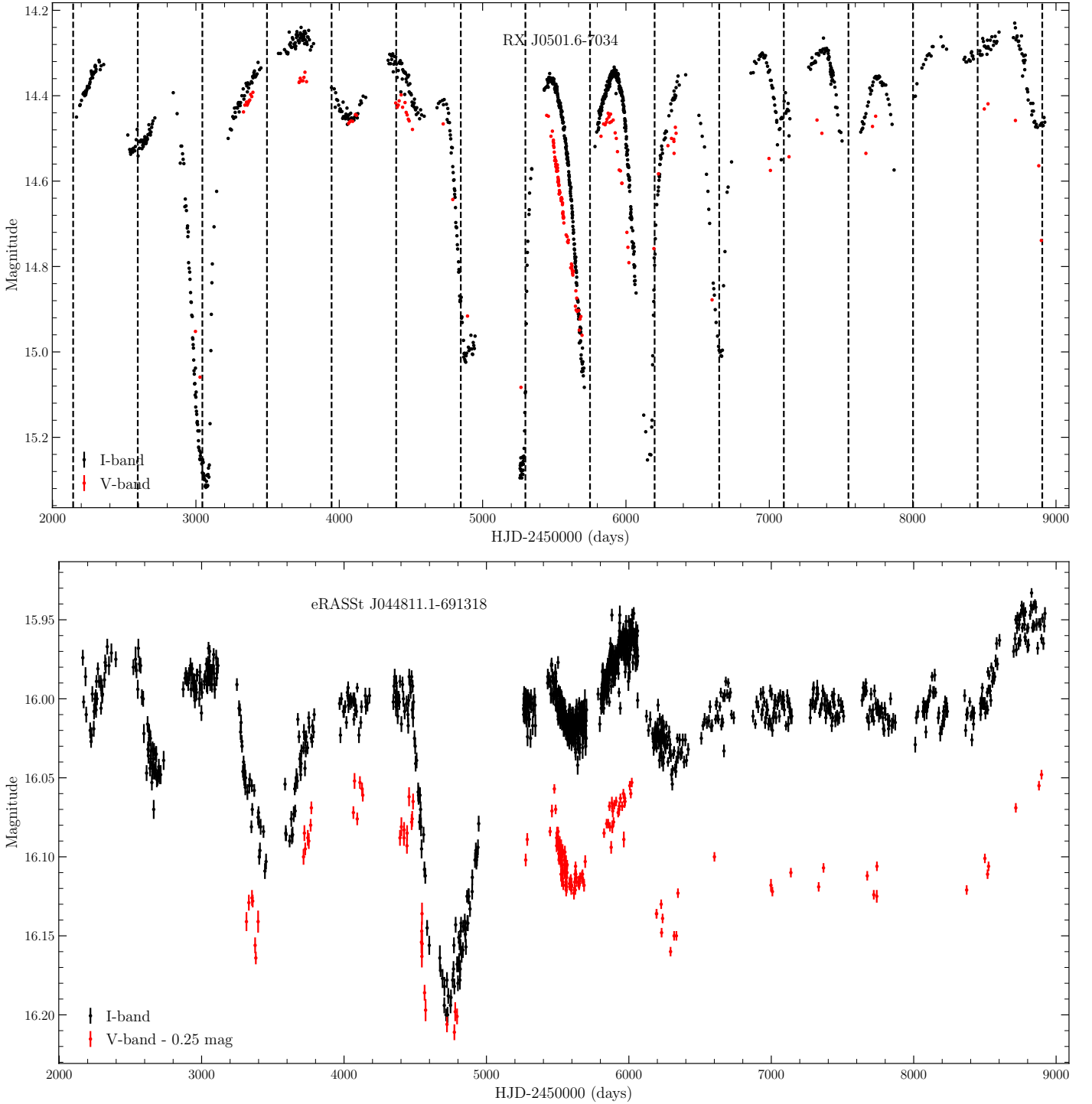


Fig. 7. I-band light curves (black) of RX J0501.6–7034 (top; between 2001 September 14 and 2020 March 13) and eRASSt J044811.1–691318 (bottom; 2001 September 13 to 2020 March 13) from OGLE phases III and IV. V-band measurements are available for both systems and shown in red. The vertical dashed lines in the top panel are separated by 450.7 days, the period indicated by the LS periodogram analysis.

It remains unclear if any of the suggested theories to explain the bimodality seen from the SMC by different types of supernovae (Knigge et al. 2011) or different accretion modes (Cheng et al. 2014) can also explain a smoother period distribution as possibly seen in the LMC.

To investigate the long-term X-ray light curve of the three BeXRBs we used the HIGh-energy LIght curve GeneraTOR (HILIGT; König et al. 2022; Saxton et al. 2022)² to search for

serendipitous observations with *XMM-Newton* and *Swift*. From the available spectral models to convert count rates to fluxes we used a power law with photon index 1.0 and an absorption column density of 10^{21} cm^{-2} . We converted the HILIGT 0.2–12 keV fluxes to the 0.2–10 keV band by re-normalising them to the values obtained from our spectral fits to the *XMM-Newton* spectra. The tool provides upper limits (2σ) when the source was not detected. We excluded *ROSAT* values due to its limited energy

² <http://xmmuls.esac.esa.int/upperlimitserver/>

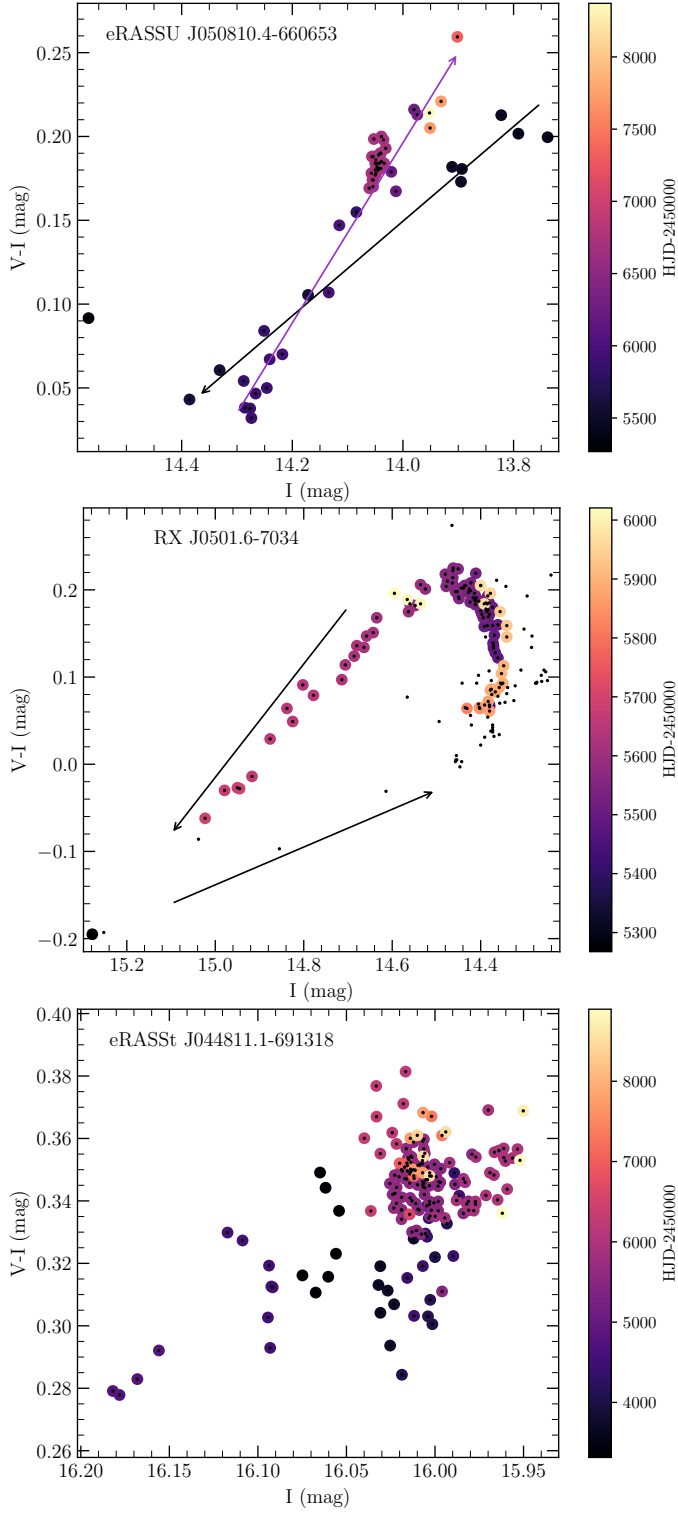


Fig. 8. OGLE V-I colour index as a function of I for eRASSU J050810.4–660653 (*top*), RX J0501.6–7034 (*middle*), and eRASSJ044811.1–691318 (*bottom*). The I values are interpolated to the times of the V-band observations. Due to the fast brightness changes seen from RX J0501.6–7034 the interpolated I values are only used when an I measurement exists within five days of the V-band observation.

band. In the following, we further discuss our results from the sources individually.

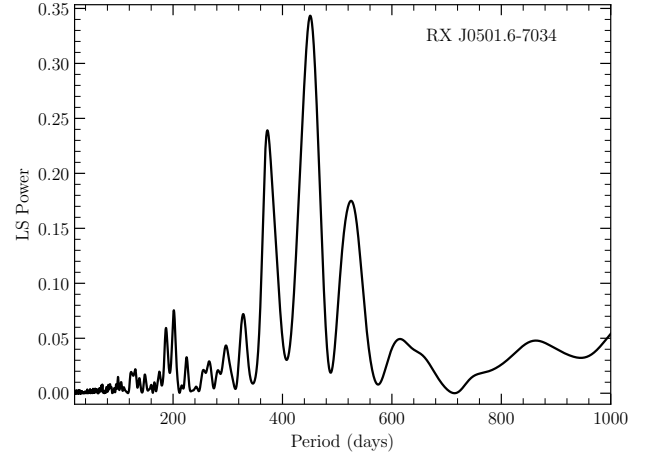


Fig. 9. Lomb-Scargle periodogram of the OGLE I-band light curve of RX J0501.6–7034. The strongest signal is found at a period of 450.7 days.

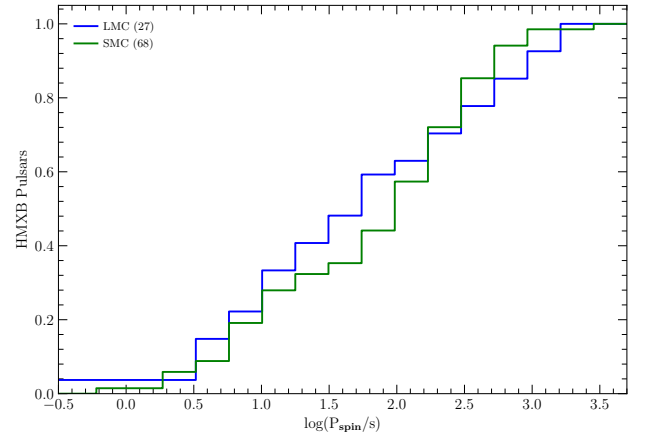


Fig. 10. Normalised cumulative spin period distribution of HMXB pulsars in the LMC and SMC.

4.1. eRASSU J050810.4–660653

While most HMXBs in the north of the LMC are located in or near the well-observed supergiant shell LMC 4, this new BeXRB was found further west between the supergiant shells LMC 1 and LMC 5 (Meaburn 1980). The position of eRASSU J050810.4–660653 was not covered by earlier *XMM-Newton* pointed observations, nor by *Swift*. HILIGT lists 20 *XMM-Newton* slews across the position of eRASSU J050810.4–660653, which resulted in six detections, four of these close in time to the ToO observation. During one of them (on 2021 February 14) the highest flux was measured with $2.5 \times 10^{-11} \text{ erg cm}^{-2} \text{ s}^{-1}$ while the lowest flux level was inferred from the eRASS1-eRASS2 scans (see Fig. 11), resulting in a flux ratio of $15.6^{+7.8}_{-5.6}$. This is typical for persistent low-luminosity BeXRBs that do not exhibit large outbursts (Haberl & Sturm 2016) and this behaviour is most likely explained by a wide and nearly circular neutron star orbit (La Palombara et al. 2013). Several such systems were recently discovered in the LMC (Haberl et al. 2022b; Maitra et al. 2023).

4.2. RX J0501.6–7034

RX J0501.6–7034 (CAL 9) was discovered with the *Einstein* observatory with a 0.15–4.5 keV luminosity of $\sim 4 \times 10^{35} \text{ erg s}^{-1}$. Although this estimate is only accurate to a factor of two (due

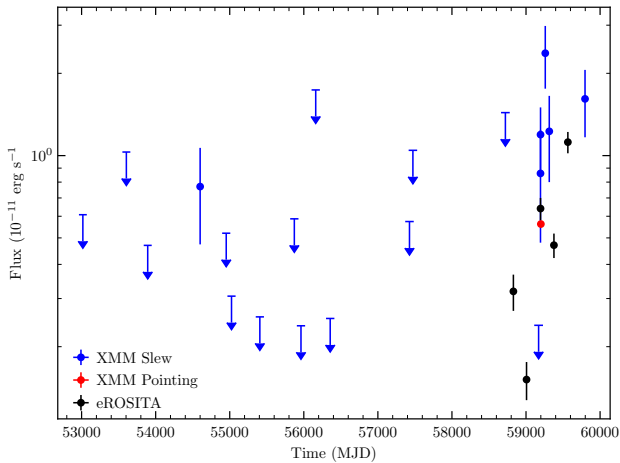


Fig. 11. Long-term X-ray light curve of eRASSU J050810.4–660653 for the 0.2–10 keV band. Our *XMM-Newton* ToO observation is marked in red.

to a model-dependent count rate conversion), it is within the range observed during the eROSITA and our *XMM-Newton* ToO observations. Using HILIGT, we found 11 *XMM-Newton* slews across RX J0501.6–7034. During a slew on 2005 May 23, the highest flux was recorded with $1.3 \times 10^{-11} \text{ erg cm}^{-2} \text{ s}^{-1}$, while the lowest flux was measured at $2.3 \times 10^{-14} \text{ erg cm}^{-2} \text{ s}^{-1}$ from an *XMM-Newton* pointed observation on 2014 November 20 (see Fig. 12), resulting in a flux ratio of 550^{+520}_{-250} . The position of RX J0501.6–7034 was also covered by 23 *Swift*/XRT observations. Five detections and 18 upper limits for the flux were all between the minimum and maximum flux seen by *XMM-Newton*. The long-term X-ray light curve demonstrates RX J0501.6–7034 as a highly variable BeXRB. Together with the relatively short spin period of the neutron star, the high variability of at least a factor of 300 is in line with the anti-correlation between these two measured variables found by Haberl & Sturm (2016) from BeXRB pulsars in the SMC.

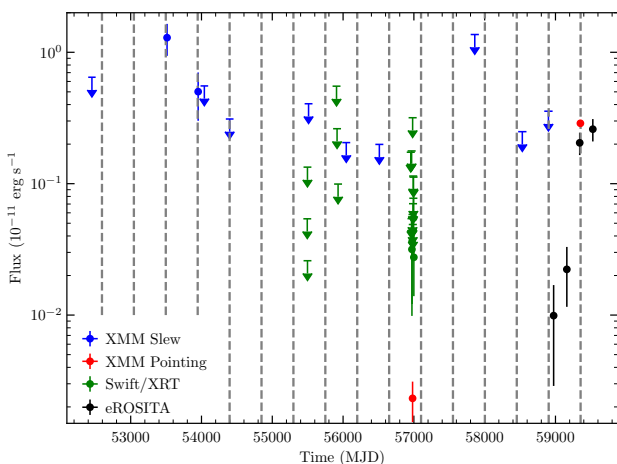


Fig. 12. Long-term X-ray (0.2–10 keV) light curve of RX J0501.6–7034. The last red data point marks our *XMM-Newton* ToO observation. The vertical dashed lines mark the times near expected optical minima as seen in Fig. 7 (top panel).

In the OGLE light curves of RX J0501.6–7034 (Fig. 7, top), six extremely deep dips were observed in which the system faded by about one magnitude, while other variations had typical amplitudes of 0.2 mag. These brightness changes repeat nearly periodic every ~ 451 days. However, the sharp deep dips do not occur

always strictly at the same phases and shift slightly with time. Such a quasi-periodic behaviour suggests a binary orbital period of about 451 days, with additional effects originating in the interaction of the neutron star with the circum-stellar disc. Such behaviour was also observed from other BeXRBs in the Magellanic Clouds and could be caused by disc truncation, disc precession, or misalignment between the disc and the orbital plane (Martin et al. 2011; Okazaki 2012; Treiber et al. 2021).

Unfortunately, no X-ray measurements are available during the six deep optical dips. However, the highest X-ray fluxes were detected at phases when dips were expected, but did not occur. In particular, during the first two *XMM-Newton* slew detections the system stayed optically bright. On the other hand, lowest flux measurements are found between dip phases. This suggests the dips occur at the periastron passage of the neutron star, which is also likely to cause the dips. The additional long-term effects, as described in the previous paragraph, are then likely to be responsible for the appearance and depth of the dips in the optical light curves.

A similar hysteresis behaviour with closed loops as shown by RX J0501.6–7034 in the colour-magnitude diagram (Fig. 8) was seen from XMMU J010331.7–730144 (Monageng et al. 2020). The authors discuss periodic mass loss from the Be star to be responsible for the quasi-periodicity of the outbursts and also for the colour-magnitude hysteresis seen from XMMU J010331.7–730144. In their picture, the optically thick inner part of a truncated disc (blue) is removed faster than the outer part (optically thinner, redder) after the mass outflow from the Be star has stopped. The authors argue that the long periodicity of ~ 1200 days from XMMU J010331.7–730144 is unusual for an orbital period, particularly given the relatively small EW of the H α line, which suggests a short orbital period according to the EW - orbital period correlation seen from BeXRBs (Reig et al. 1997). However, XMMU J010331.7–730144 and RX J0501.6–7034 also show differences in their OGLE light curves. XMMU J010331.7–730144 is characterised by extreme outbursts with amplitudes of ~ 1 mag in the I-band, which occur quasi-periodically every ~ 1200 days, while RX J0501.6–7034 shows dips with brightness decreases by a similar amount and on a shorter timescale of ~ 451 days. The shorter period found for RX J0501.6–7034 together with a larger H α EW ($\sim 10.4 \text{ \AA}$ measured in February 2001, Riquelme et al. 2012) may favour the orbital period scenario. In that case the neutron star truncates the outer disc when approaching periastron. This leads to decreasing disc brightness and bluer colour, as indicated by the upper arrow in the middle panel of Fig. 8. After periastron passage, the neutron star departs from the disc, which is then replenished, getting brighter and redder, following the path indicated by the lower arrow.

4.3. eRASSU J044811.1–691318

This new BeXRB long-period pulsar (784 s) is located at the rim of the supergiant shell LMC 7 in the west of the LMC, where two others had been found: XMMU J045736.9–692727 (318 s, Haberl et al. 2022b) and Swift J045106.8–694803 (187 s, Klus et al. 2013). In particular, eRASSU J044811.1–691318 is among the X-ray faintest BeXRBs in the Magellanic Clouds. From 13 *XMM-Newton* slew observations, only the upper limits of typically a few $10^{-12} \text{ erg cm}^{-2} \text{ s}^{-1}$ have been inferred, similar or above the detections with eROSITA and *XMM-Newton* (ToO). HILIGT lists two deep archival *XMM-Newton* observations on 2017 September 28 with 0.2–10 keV flux of $(1.4 \pm 0.6) \times 10^{-14} \text{ erg}$

$\text{cm}^{-2} \text{ s}^{-1}$ and 2019 October 15 with $(2.0 \pm 0.6) \times 10^{-14} \text{ erg cm}^{-2} \text{ s}^{-1}$. With the maximum observed flux during eROSITA, the variability is a factor of ~ 100 , but given the large flux uncertainties, it is not very well constrained (100^{+210}_{-70}). Nevertheless, this variability is still within the range observed from BeXRB pulsars with long spin periods of nearly 1000 s (Haberl & Sturm 2016).

5. Conclusions

The discovery of two new Be/X-ray binary systems in eROSITA data and the detection of pulsations from RX J0501.6–7034 increase the number of Be/X-ray binary pulsars in the LMC to 27. Their spin-period distribution does not show the bimodal characteristics of the SMC pulsars, but more LMC systems are still needed to test if this difference is significant.

Acknowledgements. This work is based on data from eROSITA, the soft X-ray instrument aboard *SRG*, a joint Russian-German science mission supported by the Russian Space Agency (Roskosmos), in the interests of the Russian Academy of Sciences represented by its Space Research Institute (IKI), and the Deutsches Zentrum für Luft- und Raumfahrt (DLR). The *SRG* spacecraft was built by Lavochkin Association (NPOL) and its subcontractors, and is operated by NPOL with support from the Max Planck Institute for Extraterrestrial Physics (MPE). The development and construction of the eROSITA X-ray instrument was led by MPE, with contributions from the Dr. Karl Remeis Observatory Bamberg & ECAP (FAU Erlangen-Nürnberg), the University of Hamburg Observatory, the Leibniz Institute for Astrophysics Potsdam (AIP), and the Institute for Astronomy and Astrophysics of the University of Tübingen, with the support of DLR and the Max Planck Society. The Argelander Institute for Astronomy of the University of Bonn and the Ludwig Maximilians Universität Munich also participated in the science preparation for eROSITA. The eROSITA data shown here were processed using the eSASS/NRTA software system developed by the German eROSITA consortium. This work used observations obtained with *XMM-Newton*, an ESA science mission with instruments and contributions directly funded by ESA Member States and NASA. The *XMM-Newton* project is supported by the DLR and the Max Planck Society. This research has made use of the VizieR catalogue access tool, CDS, Strasbourg, France. The original description of the VizieR service was published in A&AS 143, 23. This work has made use of data from the European Space Agency (ESA) mission *Gaia* (<https://www.cosmos.esa.int/gaia>), processed by the *Gaia* Data Processing and Analysis Consortium (DPAC, <https://www.cosmos.esa.int/web/gaia/dpac/consortium>). Funding for the DPAC has been provided by national institutions, in particular the institutions participating in the *Gaia* Multilateral Agreement. LD acknowledges support from the Bundesministerium für Wirtschaft und Energie through the DLR grant FKZ 50 QR 2102.

References

- Arnaud, K. A. 1996, in ASP Conf. Ser. 101: Astronomical Data Analysis Software and Systems V, 17
- Brunner, H., Liu, T., Lamer, G., et al. 2022, A&A, 661, A1
- Buckley, D. A. H., Swart, G. P., & Meiring, J. G. 2006, in Society of Photo-Optical Instrumentation Engineers (SPIE) Conference Series, Vol. 6267, Society of Photo-Optical Instrumentation Engineers (SPIE) Conference Series, ed. L. M. Stepp, 62670Z
- Burgh, E. B., Nordsieck, K. H., Kobulnicky, H. A., et al. 2003, in Society of Photo-Optical Instrumentation Engineers (SPIE) Conference Series, Vol. 4841, Instrument Design and Performance for Optical/Infrared Ground-based Telescopes, ed. M. Iye & A. F. M. Moorwood, 1463–1471
- Cash, W. 1979, ApJ, 228, 939
- Cheng, Z.-Q., Shao, Y., & Li, X.-D. 2014, ApJ, 786, 128
- Cowley, A. P., Crampton, D., Hutchings, J. B., et al. 1984, ApJ, 286, 196
- Crampton, D., Cowley, A. P., Thompson, I. B., & Hutchings, J. B. 1985, AJ, 90, 43
- Dickey, J. M. & Lockman, F. J. 1990, ARA&A, 28, 215
- Gaia Collaboration, Brown, A. G. A., Vallenari, A., et al. 2021, A&A, 649, A1
- Gaia Collaboration, Prusti, T., de Bruijne, J. H. J., et al. 2016, A&A, 595, A1
- Gregory, P. C. & Lored, T. J. 1996, ApJ, 473, 1059
- Grundstrom, E. D. & Gies, D. R. 2006, ApJ, 651, L53
- Haberl, F., Eger, P., & Pietsch, W. 2008, A&A, 489, 327
- Haberl, F., Maitra, C., Carpano, S., et al. 2022a, A&A, 661, A25
- Haberl, F., Maitra, C., Carpano, S., et al. 2020, The Astronomer’s Telegram, 13609, 1
- Haberl, F., Maitra, C., Vasilopoulos, G., et al. 2022b, A&A, 662, A22
- Haberl, F., Salganik, A., Maitra, C., et al. 2021, The Astronomer’s Telegram, 15133, 1
- Haberl, F. & Sturm, R. 2016, A&A, 586, A81
- Klus, H., Bartlett, E. S., Bird, A. J., et al. 2013, MNRAS, 428, 3607
- Knigge, C., Coe, M. J., & Podsiadlowski, P. 2011, Nature, 479, 372
- König, O., Saxton, R. D., Kretschmar, P., et al. 2022, Astronomy and Computing, 38, 100529
- La Palombara, N., Mereghetti, S., Sidoli, L., Tiengo, A., & Esposito, P. 2013, Mem. Soc. Astron. Italiana, 84, 626
- Lomb, N. R. 1976, Ap&SS, 39, 447
- Long, K. S., Helfand, D. J., & Grabelsky, D. A. 1981, ApJ, 248, 925
- Luck, R. E., Moffett, T. J., Barnes, Thomas G., I., & Gieren, W. P. 1998, AJ, 115, 605
- Maitra, C., Haberl, F., Carpano, S., et al. 2020a, The Astronomer’s Telegram, 13610, 1
- Maitra, C., Haberl, F., Koenig, O., et al. 2020b, The Astronomer’s Telegram, 13650, 1
- Maitra, C., Haberl, F., Vasilopoulos, G., et al. 2021, A&A, 647, A8
- Maitra, C., Kaltenbrunner, D., Haberl, F., et al. 2023, A&A, 669, A30
- Martin, R. G., Pringle, J. E., Tout, C. A., & Lubow, S. H. 2011, MNRAS, 416, 2827
- Massey, P. 2002, ApJS, 141, 81
- Meaburn, J. 1980, MNRAS, 192, 365
- Monageng, I. M., Coe, M. J., Buckley, D. A. H., et al. 2020, MNRAS, 496, 3615
- Negueruela, I. & Coe, M. J. 2002, A&A, 385, 517
- Okazaki, A. T. 2012, in Astronomical Society of the Pacific Conference Series, Vol. 464, Circumstellar Dynamics at High Resolution, ed. A. C. Carciofi & T. Rivinius, 177
- Pavlinksky, M., Tkachenko, A., Levin, V., et al. 2021, A&A, 650, A42
- Predehl, P., Andritschke, R., Arefiev, V., et al. 2021, A&A, 647, A1
- Reig, P., Fabregat, J., & Coe, M. J. 1997, A&A, 322, 193
- Riquelme, M. S., Torrejón, J. M., & Negueruela, I. 2012, A&A, 539, A114
- Rolleston, W. R. J., Trundle, C., & Dufton, P. L. 2002, A&A, 396, 53
- Salganik, A., Tsygankov, S. S., Lutovinov, A. A., et al. 2022, MNRAS, 514, 4018
- Saxton, R. D., König, O., Descalzo, M., et al. 2022, Astronomy and Computing, 38, 100531
- Scargle, J. D. 1982, ApJ, 263, 835
- Schmidtke, P. C., Cowley, A. P., Frattare, L. M., et al. 1994, PASP, 106, 843
- Skrutskie, M. F., Cutri, R. M., Stiening, R., et al. 2006, AJ, 131, 1163
- Strüder, L., Briel, U., Dennerl, K., et al. 2001, A&A, 365, L18
- Sturm, R., Haberl, F., Pietsch, W., et al. 2013, A&A, 558, A3
- Treiber, H., Vasilopoulos, G., Bailyn, C. D., et al. 2021, MNRAS, 503, 6187
- Turner, M. J. L., Abbey, A., Arnaud, M., et al. 2001, A&A, 365, L27
- Udalski, A., Szymanski, M. K., Soszynski, I., & Poleski, R. 2008, Acta Astron., 58, 69
- Udalski, A., Szymański, M. K., & Szymański, G. 2015, Acta Astron., 65, 1
- Vasilopoulos, G., Maggi, P., Haberl, F., et al. 2013, A&A, 558, A74
- Vasilopoulos, G., Zezas, A., Antoniou, V., & Haberl, F. 2017, MNRAS, 470, 4354
- Verner, D. A., Ferland, G. J., Korista, K. T., & Yakovlev, D. G. 1996, ApJ, 465, 487
- Wilms, J., Allen, A., & McCray, R. 2000, ApJ, 542, 914
- Zaritsky, D., Harris, J., Thompson, I. B., & Grebel, E. K. 2004, AJ, 128, 1606

Appendix A: eROSITA light curves

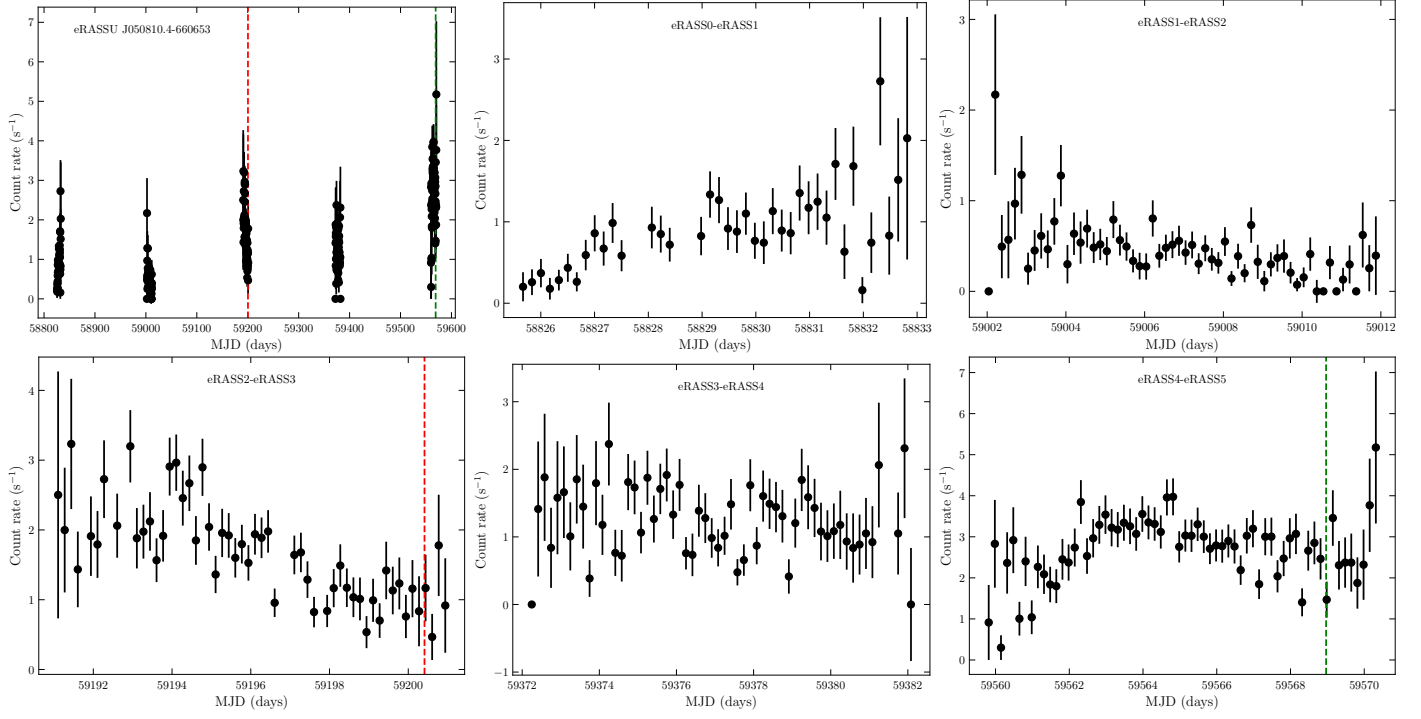


Fig. A.1. eROSITA light curve of eRASSU J050810.4–660653 in the energy band 0.2–8 keV, combining data from all TMs. Until the end of 2021, eROSITA scanned the source during five epochs (upper left). The first scans were performed during a test phase (named eRASS0) before the official start of the all-sky survey (MJD 58828) with eRASS1 and then around the formal transitions of eRASS1–eRASS2, eRASS2–eRASS3, eRASS3–eRASS4, and eRASS4–eRASS5. The red and green dashed lines mark the beginning of the *XMM-Newton* and *NuSTAR* observations (Salganik et al. 2022; Haberl et al. 2021), respectively.

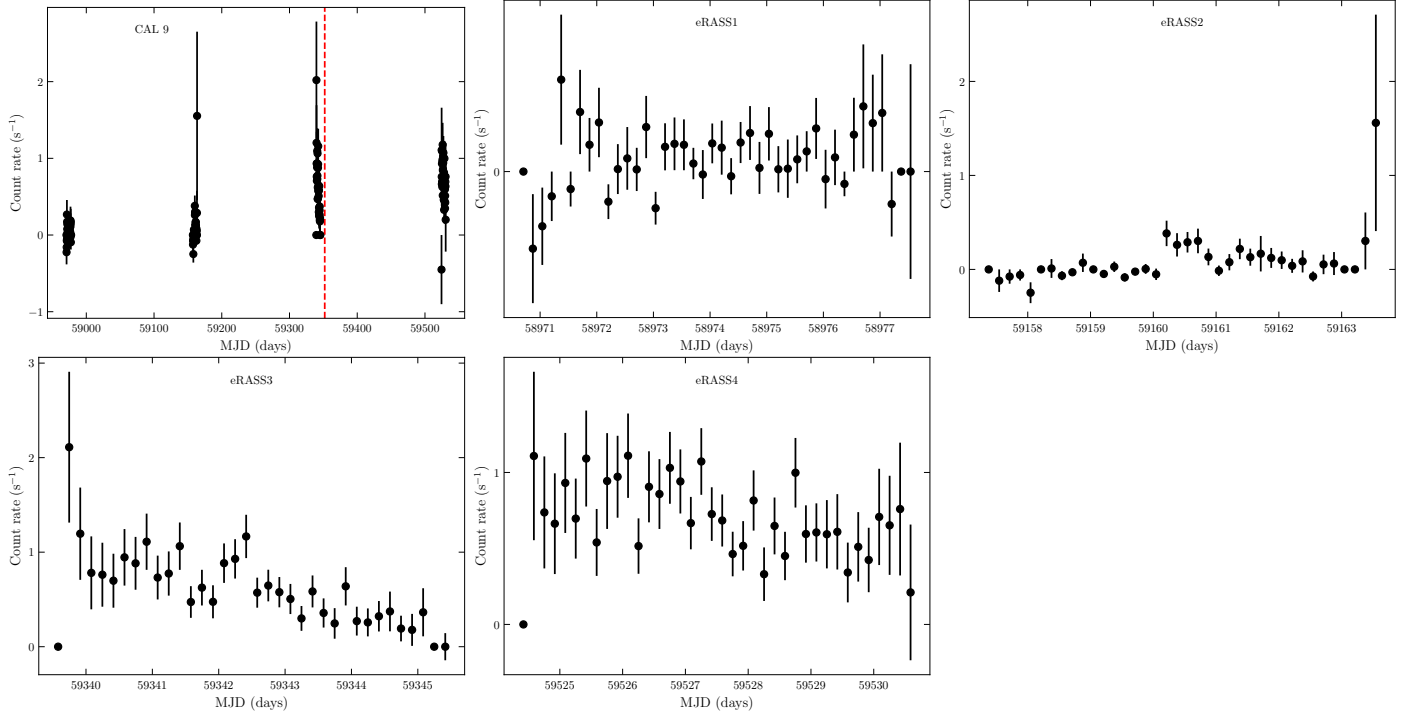


Fig. A.2. eROSITA light curve of RX J0501.6–7034, created as described in Fig. A.1. eROSITA scanned the source during eRASS1–4. Red dashed line marks the beginning of the *XMM-Newton* observation, which was performed shortly after the last source scans during eRASS3.

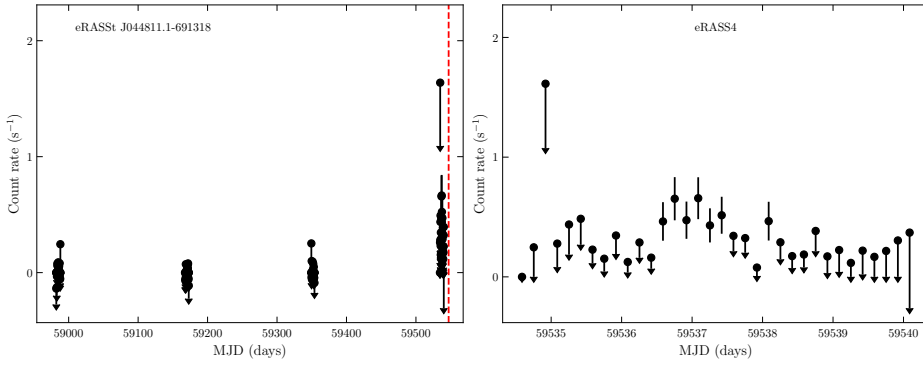


Fig. A.3. eROSITA light curve of eRASS1 J044811.1–691318, created as described in Fig. A.1. The red dashed line marks the beginning of the *XMM-Newton* observation, which was performed shortly after the last source scans during eRASS4. The source was not detected during eRASS1, 2, and 3 (the corresponding light curves are not shown).